ACS NANO
Cite This: ACS Nano 2018, 12, 836−843
www.acsnano.org

ARTICLE

Functional Two-Dimensional Coordination Polymeric Layer as a Charge Barrier in Li−S Batteries

Jing-Kai Huang,*[,†,○] Mengliu Li,[†,○] Yi Wan,[†] Sukumar Dey,[†] Mayur Ostwal,[‡] Daliang Zhang,[§] Chih-Wen Yang,[†] Chun-Jen Su,[∥] U-Ser Jeng,[∥,⊥] Jun Ming,[†] Aram Amassian,[†] Zhiping Lai,[‡] Yu Han,[‡] Sean Li,*[,▽] and Lain-Jong Li*[,†,#]

[†]KAUST Solar Center, Physical Sciences and Engineering Division, [‡]Advanced Membrane and Porous Materials Center, Physical Sciences and Engineering Division, and [§]Imaging and Characterization Core Laboratory, King Abdullah University of Science and Technology, Thuwal, 23955-6900, Kingdom of Saudi Arabia

[∥]National Synchrotron Radiation Research Center, Hsinchu, 30076, Taiwan

[⊥]Department of Chemical Engineering, National Tsing Hua University, Hsinchu 30013, Taiwan

[▽]School of Materials Science and Engineering, University of New South Wales, Sydney, New South Wales 2052, Australia

[#]Corporate Research and Chief Technology Office, Taiwan Semiconductor Manufacturing Company (TSMC), Hsinchu 30075, Taiwan

Supporting Information

ABSTRACT: **Ultrathin two-dimensional (2D) polymeric layers are capable of separating gases and molecules based on the reported size exclusion mechanism. What is equally important but missing today is an exploration of the 2D layers with charge functionality, which enables applications using the charge exclusion principle. This work demonstrates a simple and scalable method of synthesizing a free-standing 2D coordination polymer Zn_2(benzimidazolate)$_2(OH)_2$ at the air−water interface. The hydroxyl (−OH) groups are stoichiometrically coordinated and implement electrostatic charges in the 2D structures, providing powerful functionality as a charge barrier. Electrochemical performance of the Li−S battery shows that the Zn_2(benzimidazolate)$_2(OH)_2$ coordination polymer layers efficiently mitigate the polysulfide shuttling effects and largely enhance the battery capacity and cycle performance. The synthesis of the proposed coordination polymeric layers is simple, scalable, cost saving, and promising for practical use in batteries.**

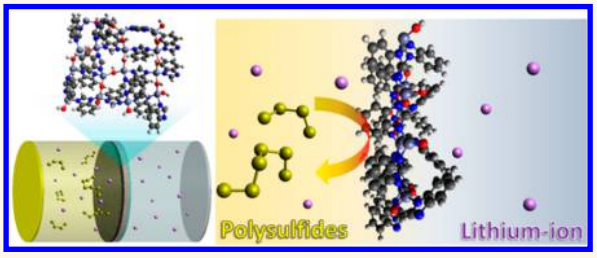

KEYWORDS: *two-dimensional materials, coordination polymers, lithium−sulfur battery, polysulfide, shuttling effect*

Two-dimensional (2D) polymeric layers have become a fascinating research topic owing to their unique physical properties by design and potential applications in sensing, catalysis, and energy conversion.[1−4] Their ultrathin feature also enables highly efficient separation of gases and molecules based on a commonly reported size exclusion mechanism.[5,6] Although decorating functional groups in covalent or noncovalent frameworks has been developed in a few works,[7,8] the 2D polymeric layers incorporated with the charge functionality are not yet achieved. "Top-down" exfoliation has been adopted to produce organic 2D nanosheets such as layered covalent organic frameworks (COFs)[1,9,10] and metal−organic frameworks (MOFs),[4−6] but the control of lateral size and layer thickness is still challenging. "Bottom-up" synthesis provides the feasibility to rationally design and construct free-standing organic 2D nanosheets in a centimeter scale for practical applications.[11−14] Among the numerous coordination structures, Zn^{2+} (or Co^{2+}) ions can coordinate with organic imidazoles in tetrahedron units, making it feasible to form 2D silicate-like structures.[5,15] However, a simple method to introduce functional groups to the structure without changing the 2D geometry is still not available. Here, we demonstrate a simple, room-temperature, and scalable synthesis of free-standing and nanometer-thin zinc benzimidazolate coordination polymer (ZBCP) layers on water surfaces, where the desired hydroxyl (−OH) groups with charge functionality are stoichiometrically coordinated into the 2D structures, characterized as $Zn_2(Bim)_2(OH)_2$. In various separation technologies,[16−21] electrostatic shield is a noticeable mechanism.[22−24] Therefore, the incorporation of hydroxyl

Received: November 20, 2017
Accepted: January 4, 2018
Published: January 4, 2018

Downloaded via SYNCHROTRON RADIATION RESEARCH on January 21, 2019 at 04:01:59 (UTC).
See https://pubs.acs.org/sharingguidelines for options on how to legitimately share published articles.

© 2018 American Chemical Society

DOI: 10.1021/acsnano.7b08223
ACS Nano 2018, 12, 836−843

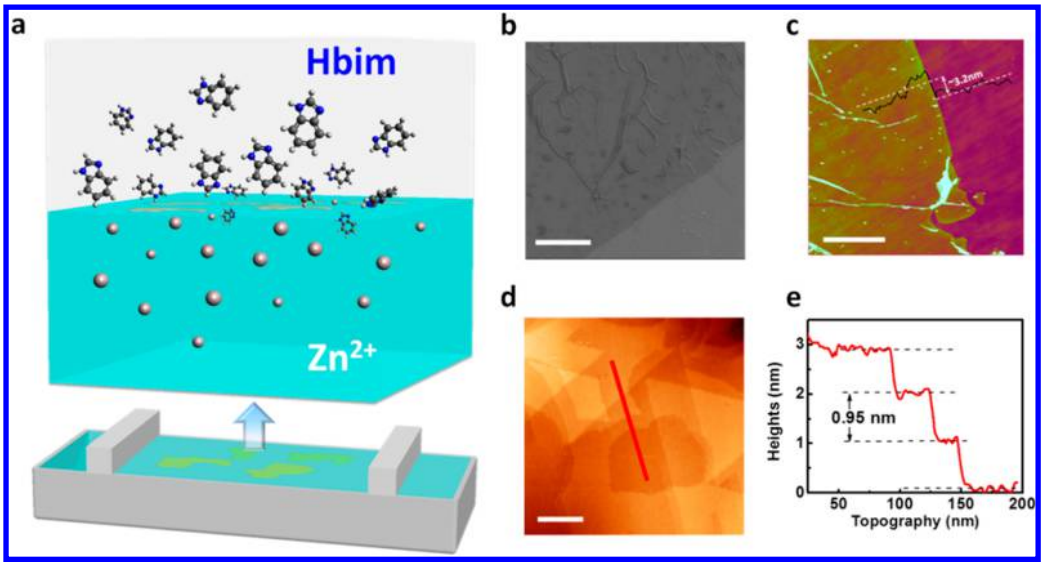

Figure 1. Synthesis and morphological characterizations of the ZBCP layers. (a) Schematic illustration for the preparation of large area ZBCP layers at air−water surfaces of a Langmuir trough. (b) SEM image of the ZBCP transferred onto a 300 nm SiO_2/Si substrate, where the wrinkles were formed during the transfer process. Scale bar: 50 μm. (c) Tapping-mode AFM topographical image of the ZBCP on a 300 nm SiO_2/Si substrate and the corresponding cross-sectional height profile demonstrating its ultrathin feature (~3 nm). Scale bars: 10 μm. (d) STM image of the small domain ZBCP on a gold (111) substrate. Scale bars: 75 nm. (e) Height profile of the nanosheets along the red line marked in (d).

groups introduces electrostatic charges in the 2D layers, making it an effective charge barrier to the transport of negative ions in basic solutions, a robust functionality that had not been achieved to date in ultrathin 2D layers. This is shown to be a significant breakthrough in next-generation Li−S batteries, where the notorious sulfur shuttling effect is shown to be suppressed in our experiments.[25]

RESULTS AND DISCUSSION

Synthesis and Morphology of the ZBCP. Figure 1a depicts the method of synthesizing large-area and free-standing two-dimensional (2D) polymeric layers based on zinc(II) benzimidazolate complex on the water surface of a Langmuir trough. A toluene solution of benzimidazole (HBim) was gently spread on top of an aqueous solution of zinc(II) acetylacetonate [$Zn(acac)_2$] using a micropipette (the details are illustrated in the Materials and Methods). The polymerization of Zn^{2+} ion and HBim occurred in ambient conditions, and then the products were compressed to a surface pressure of 30 mN/m, which promoted the formation of a large-area film. We note that some coordination structures of Zn^{2+} ions with HBim have been reported, but most of the results were single-phase solvent syntheses.[5,26] However, those predecessors provide a hint that the coordinating environment deeply affects the morphology of the products. Here, we utilize water/toluene heterogeneous phase and fast solvent evaporation of the toluene to produce confinement of the reaction in two dimensions, resulting in large-area 2D zinc benzimidazolate coordination polymer (ZBCP) layers on the water surface. Furthermore, because the reaction occurs in an alkaline environment resulting from dissociation of $Zn(acac)_2$, the hydroxyl groups (-OH) are also coordinated to zinc as part of the coordination system. The thickness of the ZBCP layers depends on the quantity of the added HBim solution, which was optimized to achieve a large-area, continuous, and transferrable 2D film as shown in the scanning electron microscopy (SEM) image (Figure 1b). The atomic force microscopy (AFM) topographical image and cross-sectional analysis in Figure 1c and Figure S1 reveal that the typical thickness of the obtained ZBCP layer is around 3.2 ± 0.2 nm. If a lesser quantity of HBim is added, the ZBCP layers become insufficiently strong for transfer; thus, small size flakes (few hundred nanometers to few micrometers in lateral size) are often observed (Figure S2 and Table S1). The scanning tunneling microscopy (STM) image of these small islands transferred onto a gold (111) substrate (Figure 1d and e and Figure S3) reveals that the obtained ZBCP film is actually a stacked structure of a few 2D monolayers (apparent thickness ~1 nm for each monolayer).

Spectroscopic and Structure Characterization of the ZBCP. Fourier transform infrared (FTIR) spectroscopy, X-ray photoelectron spectroscopy (XPS), X-ray fluorescence (XRF) analysis, and elemental analyzer were adopted to explore the chemical structure of the obtained ZBCP film. Most of the IR vibrational modes in Figure 2a are attributed to the benzimidazolate (Bim) including the entire ring stretching or bending at 600−1500 cm^{-1}, the =C−H stretching of aromatics at 3068 and 3032 cm^{-1}, and the C−C stretching of the aromatic ring at 1611 and 1465 cm^{-1}.[27] The presence of the Zn−N stretching at 421 cm^{-1} and the translation mode of Zn−OH at 465 cm^{-1} proves that zinc(II) ions form coordination bonds with Bim and hydroxyl groups.[28,29] The observation of bending modes at 850 and 1015 cm^{-1} and the single Zn−OH deformation band at around 1520 cm^{-1} further corroborates the formation of the Zn−OH bonds.[29,30] Furthermore, the N−H vibration mode of free HBim located at 628 cm^{-1} disappears after coordination with the zinc(II) ions.[27] These results suggest that the ZBCP layer is a coordinated system of zinc(II), benzimidazolate, and hydroxyl groups. Figure 2b displays the XPS spectra of N 1s and O 1s for the ZBCP layers. Two N 1s peaks from HBim corresponding to nonprotonated (399 eV) and protonated (401 eV) nitrogen were identified.[31] The nonprotonated nitrogen dominates the whole peak (96.53%), indicating that the pyrrole nitrogen (−NH−) in HBim has

DOI: 10.1021/acsnano.7b08223
ACS Nano 2018, 12, 836−843

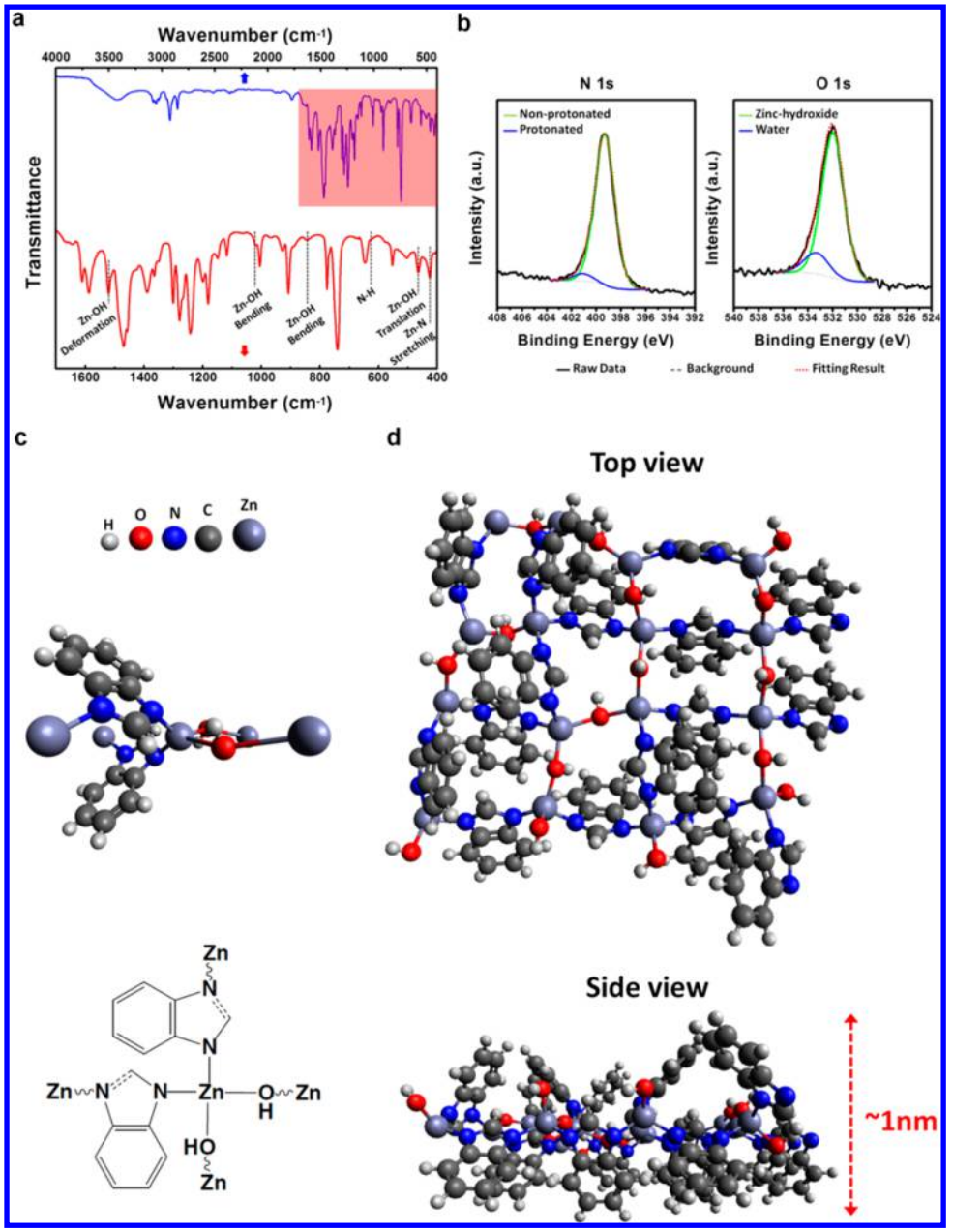

Figure 2. Spectroscopic characterization and molecular structure of the ZBCP. (a) Full and zoom-in FTIR spectra of the ZBCP film. (b) XPS spectra of N 1s (left) and O 1s (right) of the ZBCP film. (c) Tetrahedral unit of $Zn_2(Bim)_2(OH)_2$ is presented to illustrate the coordination environment of Zn atoms. (d) Top and side views of the proposed structure of $Zn_2(Bim)_2(OH)_2$.

been deprotonated and coordinated to zinc(II) ions. This conclusion is supported by the absence of N−H vibration mode in the FTIR spectrum (Figure 2a). The predominant peak in the O 1s spectrum with a binding energy of 532 eV is originated from the zinc hydroxide bond (Zn−OH) in the ZBCP, whereas the weak peak at 533.3 eV is correlated to a trace amount of residual moisture.[32,33] For the chemical composition of the ZBCP layer to be quantitatively defined, XRF and elemental analysis were performed. Zinc is confirmed as the major metal component (>99.6 at. %, Figure S4) by XRF measurements. The elemental analysis (details in Figure S5 and Table S2) reveals the composition of the ZBCP layers as C, 42.11%; H, 3.34%; N, 13.66%; O, 8.46%. In other words, the atomic composition matches well to the chemical formula $Zn_2(Bim)_2(OH)_2$.

The transmission electron microscopy (TEM), selected area electron diffraction (SAED), and grazing incidence X-ray diffraction (GI-XRD) do not reveal any evidence of a crystalline structure (Figures S6 and S7), suggesting that the ZBCP layers may be amorphous in the in-plane direction. Owing to its amorphous nature, there should be no well-defined pore structures within the ZBCP. The porosity analysis consequently did not show pronounced porosity in the ZBCP (pore structure analysis in Figures S8 and S9). Furthermore, the amorphous structure actually gives better tolerance to mechanical stress compared with that of a crystalline film, which is advantageous for applications. This can be inferred from the existing wrinkles but not cracks in the ZBCP thin film shown in SEM, OM, and AFM images (Figure 1b and c and Figures S1 and S10). Taking the FTIR and XPS results together with the confirmed formula $Zn_2(Bim)_2(OH)_2$, the structure of ZBCP is proposed in Figure

DOI: 10.1021/acsnano.7b08223
ACS Nano 2018, 12, 836−843

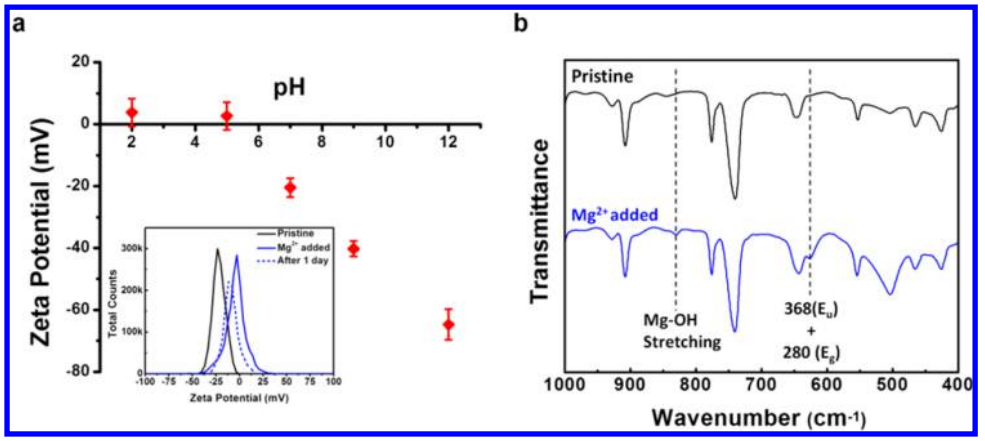

Figure 3. Electrostatic charge property of the ZBCP. (a) Zeta potential values of the ZBCP dispersed in deionized water with various pH values. The inset shows that the zeta potential of the intrinsic ZBCP decreases after adding Mg^{2+} ions. (b) FTIR spectra of the ZBCP before and after adding Mg^{2+} ions, where the formation of Mg−OH bonds results in the reduction of the net electrical charges in the ZBCP.

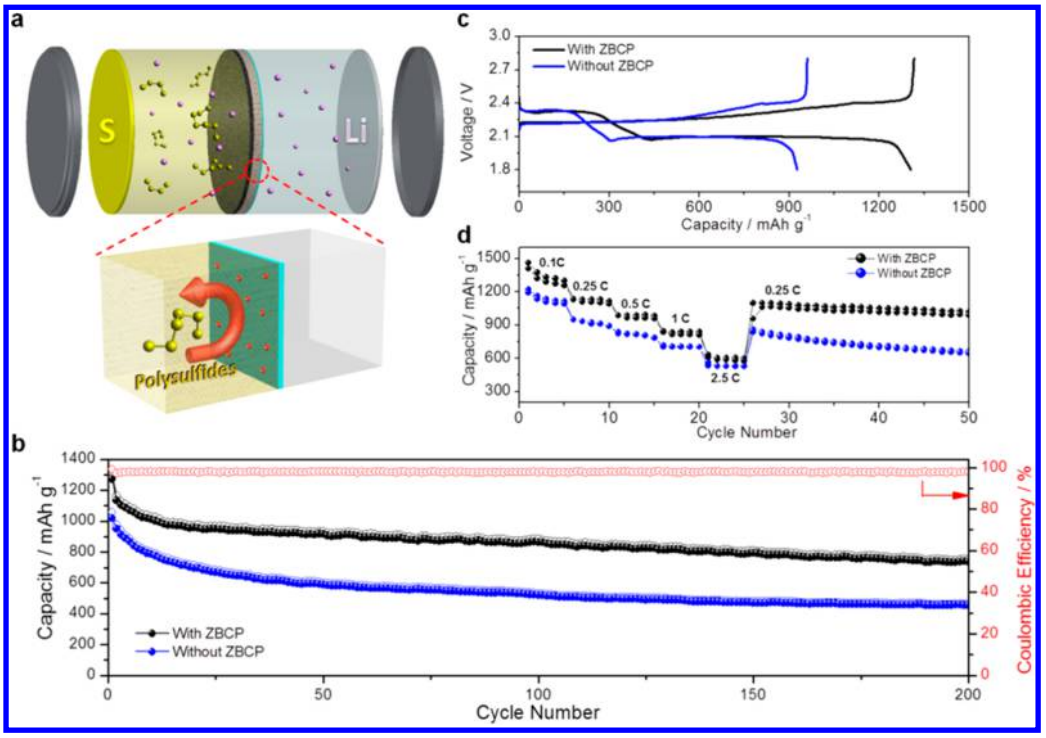

Figure 4. Electrochemical performance of the Li−S batteries with and without ZBCP. (a) Schematic of a ZBCP-coated separator and the charge repulsion operation of the ZBCP layer. (b) Cycling performance of the batteries using the separator with and without ZBCP coating at 0.25 C. (c) First cycle charge−discharge curves for the batteries using different separators. (d) Rate capacity and cycling retention of the battery using the separator with and without ZBCP coating.

2c. Each zinc(II) ion is coordinated with two benzimidazolates and two hydroxyl groups to form a tetrahedral unit. The extension of the unit allows the formation of a planar polymer (Figure 2d) as evidenced by the STM image in Figure 1d. Furthermore, contact-angle measurements show that the front side (facing air) and the back side (facing aqua) of the ZBCP nanosheets are hydrophobic (Figure S11). The result reveals that aromatic rings within benzimidazolates should dominate the ZBCP's outer surfaces and the hydroxyl groups are in the center part of the film as proposed. For further proving that the ZBCP is stably coordinated as a planar rather than a linear polymer structure, it was subjected to solubility tests in various solvents for more than 24 h, where the ZBCP does not dissolve in most of the solvents including ethanol, acetone, toluene, NMP, DMF, and water (pH from 7 to 12) except in acid aqua (Table S3) due to instability of Zn−N and Zn−O bonds in acids.[34,35] The simulated $Zn_2(Bim)_2(OH)_2$ structure was shown after energy minimization using molecular dynamics, and the thickness of the ZBCP polymeric monolayer (1 nm) agrees well with the STM results.

Electrostatic Charge Property of the ZBCP. The electrostatic potential of material surfaces can be probed by zeta potential measurements: increasing zeta potential results in larger surface potential of a charged surface.[36] For performing the zeta potential measurement, the ZBCP layers were broken into small pieces and suspended in deionized water adjusted to different pH values (Figure 3a). The intrinsic ZBCP (pH 7) is negatively charged likely due to the amphoterism of zinc

DOI: 10.1021/acsnano.7b08223
ACS Nano 2018, 12, 836−843

hydroxides, where the zinc hydroxides behave as Lewis acids that receive electron pairs from other hydroxides in basic solutions.[34] To verify the origin of negative charges, we introduced a small amount of Mg^{2+} ions into the solution and kept the pH value of the system at around 7. As shown in the Figure 3a inset, the zeta potential of the ZBCP decreases with Mg^{2+} addition due to the affinity of hydroxide (OH^-) to Mg^{2+} ions, meaning that the Mg^{2+} ions can passivate the hydroxyl groups in ZBCP and diminish the surface charges. The formation of Mg−OH bonding was also proven by FTIR measurements. Two peaks at 830 and 625 cm^{-1} are assigned to the Mg−OH stretching mode and the combination modes of E_u (368 cm^{-1}) and E_g (280 cm^{-1}), respectively (Figure 3b).[29,37,38] The zeta potential dependence on pH value and Mg^{2+} passivation clearly indicate that the surface electrostatic property is attributed to the amphoteric property of hydroxyl groups in the ZBCP.

Electrochemical Performance of the Li−S Batteries with the ZBCP. The inclusion of a vast number of hydroxyl groups in the layered ZBCP presents great potential in applications requiring charge filters such as an ultrathin charge barrier membrane for Li−S batteries to mitigate the notorious polysulfide shuttling effect. The shuttling effect is a major issue due to the migration of dissolved (negatively charged) polysulfides to the lithium anode, which forms an insoluble Li_2S, causing significant capacity degradation.[39−41] Figure 4a illustrates the configuration of the battery and the schematics for stopping the polysulfides with the charge barrier. In our experiments, the commonly used glass fiber (GF) separator coated with a layer of carbon nanotubes (CNT) is adopted as the baseline separator (denoted as GF/CNT). Note that the main function of CNTs is to enhance the conductivity for the sulfur cathode and also to help suppress the polysulfide migration as the first barrier.[20] The large-area ZBCP layers (~10 nm thick; Figure S10) were transferred onto a GF/CNT separator to form a ZBCP/GF/CNT structure. The electrochemical characteristics of the Li−S batteries integrated with and without the ZBCP charge barrier were examined. The galvanostatic cycling tests were performed at 0.25 C at the voltage window of 1.8−2.8 V. Figure 4b shows that the initial capacity of the battery with ZBCP layers could reach 1272 mAh g^{-1}, whereas the one without ZBCP shows a lower capacity of 927 mAh g^{-1} (Figure 4c). Both batteries exhibit typical discharge plateaus at 2.3 and 2.1 V. After 200 cycles, the battery with the ZBCP could maintain a relatively high capacity of 738 mAh g^{-1}, whereas the one without ZBCP shows obvious decay to 412 mAh g^{-1}. It is clear that the battery with the ZBCP barrier has a much higher capacity even in the first few cycles. It means that effectively more polysulfides are utilized in the batteries with a ZBCP barrier. The capacitance loss could be attributed to many different reasons including (1) self-discharge to form insoluble Li_2S before cycling and (2) the loss of S into the electrolytes because S needs to be dissolved in electrolytes for discharge/charge. The ZBCP negatively charged barrier layer actually can help to reduce both self-discharge and loss of S to the electrolyte at the anode side due to the efficient blocking of S ions from S cathode to Li anode. In addition, the C-rate performance was examined using two separators. The battery with ZBCP separator delivered capacities of 1407, 1130, 987, 842, and 610 mAh g^{-1} at 0.1, 0.25, 0.5, 1, and 2.5 C, respectively, which are much higher than the one without the ZBCP (Figure 4d and Figure S12b). Note that, under a high rate of 2.5 C, the battery ZBCP has a similar capacity with the one without ZBCP, which is because of the ultrathin property of the ZBCP layers. The outstanding capacity and stability prove the ability of the ZBCP layers for suppressing the polysulfide shuttling. Moreover, the ohmic resistance in the battery after adding a ZBCP charge barrier does not present a significant increase owing to its nanometer thickness (the detailed analysis discussed is shown in Figure S13), which is attractive for battery applications. We also like to point out that the optimized configuration for the battery is to have a lower resistance between the S cathode and the separator; therefore, CNTs facing the S cathode with the ZBCP facing the Li anodes is the preferred structure (details in Supporting Information and Figure S14).

After the charge−discharge cycling, the separators with and without ZBCP were examined by SEM, energy-dispersive X-ray analysis (EDX) mapping, and FTIR (Figures S15−S18 and Table S5), and it can be seen that the ZBCP layers remain attached on GF (Figure S15c). Moreover, the ZBCP side (Figure S17f, i, and j) clearly shows more oxygen and fewer sulfur doses than the CNT side (Figure S17a, d, and e), as proven by the elemental analysis in Table S5. The superimposed sulfur elemental mapping on the cross-sectional SEM image of the ZBCP separator (Figure S18) reveals an obvious sulfur depletion region right underneath the ZBCP layer, suggesting the strong blocking effect by the ZBCP layer. In addition, the polysulfide permeation measurements for the separators with and without ZBCP were conducted (Figure S19).[18] The brown polysulfide-containing electrolyte will diffuse into the transparent electrolyte in the outside bottle down a concentration gradient. Apparently, the transparent electrolyte using separator without ZBCP layer turned a light yellow quickly after 12 h, whereas the one with ZBCP separator has almost no color change even after 48 h. This phenomenon confirms that the ZBCP barrier has superior ability to stop the polysulfide diffusion, which is consistent with its excellent electrochemical performance.

CONCLUSIONS

In summary, we proposed a synthetic strategy to grow a large-area and transferable Zn-coordination 2D polymer, where OH functional groups and the amphoterism of zinc hydroxides play an active role in the separation/selection using the charge exclusion principle. The charge barrier feature has been integrated into the Li−S battery to mitigate the polysulfide shuttle effects by the electrostatic shield, largely promoting the Li−S capacity and cycle performance. The synthesis is simple, scalable, and cost saving, and it is anticipated that this type of functional 2D coordination polymer can soon be adopted for practical use.

MATERIALS AND METHODS

Materials. The following chemicals, including zinc(II) acetylacetonate hydrate (99.995%), benzimidazole (98%), toluene (anhydrous, 99.8%), nitric acid (ACS reagent, 70%), magnesium sulfate (≥99.99%), *N*-methylpyrrolidinone (anhydrous, 99.5%), sulfur (purum p.a., ≥99.5%), lithium foil (99.9%), bis(trifluoromethane)-sulfonimide lithium salt (LiTFSI) (99.95% trace metals basis), $LiNO_3$ (99.99% trace metals basis), 1,2-dimethoxyethane (DME) (anhydrous, 99.5%), and 1,3-dioxolane (DOL) (contains ~75 ppm BHT as inhibitor, 99%) were purchased from Sigma-Aldrich Co. LLC. Ammonium hydroxide (28.0−30.0%, w/w) was supplied from Fisher Chemical. The glass fiber separator (GC-50) was obtained from Advantec MFS, Inc. Cabon nanotubes (CNT) were purchased from

DOI: 10.1021/acsnano.7b08223
ACS Nano 2018, 12, 836−843

CNANO Company, China. Water was purified by Milli-Q purification system (Merck KGaA).

Synthesis of the ZBCP. Zinc(II) acetylacetonate (263.6 mg, 1 mmol) was dissolved in deionized water (500 mL), and the solution (pH ~8) was poured into a 240 mL trough. The benzimidazole/toluene solution was always saturated because of the low solubility of benzimidazole in toluene (~8.5 mM at room temperature).[42] Thus, the benzimidazole/toluene solution was centrifugated to remove the excess benzimidazole precipitates. Then, the clear benzimidazole/toluene solution (500 μL) was gently dropped onto the surface of zinc(II) acetylacetonate solution by micropipette. After a few minutes, the fast solvent evaporation of the toluene produced confinement of the ligands on the aqueous surface, and then polymerization occurred. The formation of the packed ZBCP thin film was followed by measuring the surface pressure−area isotherm as the surface was compressed to 30 mN/m (Figure S21), and then, the compact thin film could be deposited on various substrates. Conversely, $Zn(acac)_2$/toluene was dropped onto the HBim/water surface. However, it is hard to produce large thin sheets on surfaces due to the insufficient solubility of $Zn(acac)_2$ in toluene or insufficient dissociation of $Zn(acac)_2$ in toluene.

Characterizations of the ZBCP. AFM was performed in tapping mode with a commercial multifunction atomic force microscope (Asylum Research Oxford Instruments, Cypher ES). STM imaging was operated in a variable temperature STM (VT-STM, Omicron) under UHV conditions (5.0×10^{-10} mbar). The ZBCP nanosheets were transferred onto gold (111)/mica substrates and kept at room temperature during measurements. For STM imaging, a chemically etched polycrystalline tungsten STM tip was used, which was further cleaned by electron bombardment *in situ* in UHV. The morphology and energy-dispersive X-ray analysis (EDX) of the ZBCP was characterized by a field emission scanning electron microscope (FEI, Quanta 600). IR spectra of the studied samples were recorded in the wavenumber range 4000−400 cm^{-1} with an FTIR spectrometer (Thermo Scientific, Nicolet iS10) using samples dispersed in pure KBr pellets or ATR method. XPS measurements were carried out using a Kratos Amicus spectrometer with monochromatic Al Kα radiation. The pressure in the chamber was maintained at less than 1.0×10^{-6} mbar during the measurement. The backgrounds were all Shirley type with the Gaussian/Lorentzian line shapes, and the analyzing software was CasaXPS. XRF spectra were measured with an X-ray analytical microscope (Horiba Scientific, XGT-7200) under vacuum conditions with a Rh X-ray tube (50 kV/1 mA). Elemental analysis of the ZBCP nanosheets was obtained by an organic elemental analyzer (Thermo Scientific, FLASH 2000). Note that the elemental analysis requires large amounts of sample (2−3 mg), which means that we need to collect the film grown by LB method around 50 times to be able to perform elemental analysis one time. XRD data were collected over the 2θ range 5~40° on a Bruker D8 ADVANCE diffractometer with Cu Kα radiation (λ = 1.5406 Å, 40 kV/40 mA). GI-XRD was performed at the 23A SWASX beamline 23A with a beam of lamda = 1.24 Å at 0.2° or 2.0° incidence at the Taiwan Light Source of the National Synchrotron Radiation Research Center, Hsinchu, using a CMOS flat-panel X-ray detector C9728DK. TEM images were taken on a Cs-corrected FEI Titan Cube transmission electron microscope operated at 300 kV. SAED patterns were collected by a Gatan Ultrascan 1000xp CCD camera. Low-dose TEM images were acquired by a Gatan K2 direct-detection camera operated in electron-counting mode. For the samples to be prepared for TEM analysis, the ZBCP nanosheets were fished on lacey carbon-supported copper grids (TED PELLA, Inc.) and dried overnight. The BET surface area of the polymers was measured by nitrogen sorption at 77 K (Micrometrics ASAP 2020) and helium sorption (Horiba SA-9601 Surface Area Analyzer); the sample was degassed at 100−150 °C for 24 h before testing.

Zeta Potential Measurements. Zeta potential measurements were performed in a Zetasizer Nano ZS (Malvern Instruments Ltd.) at room temperature. For the measurement, the ZBCP $[Zn_2(Bim)_2(OH)_2]$ nanosheets (40 mg, 0.1 mmol) were dispersed in deionized water (100 mL) in an ultrasonic bath for 1 h. Nitric acid and ammonium hydroxide were used for conventional pH adjustment of aqua suspensions. The analysis was processed using a DTS1070 clear disposable folded capillary cell. For verifying the origin of surface charges, magnesium sulfate (6 mg, 0.05 mmol) was dissolved in the aqua suspension of ZBCP (100 mL) before the measurement.

Separator Coating and Cathode Preparation. The glass fiber separator was first coated with CNT paste (CNT: PVDF binder = 90:10, w/w) on one side and dried under a vacuum at 100 °C for 1 day. After drying, the separator was cut into Φ18 mm diameter round shape separators. The ZBCP was transferred on the other side for the ZBCP/GF/CNT structure (or the CNT side for ZBCP/CNT/GF structure). Then, the separator was dried again under a vacuum for 1 day at 60 °C. The transfer process was repeated 3 times to make an approximate 10 nm thick ZBCP thin film on the glass fiber separator. The sulfur powder was first mixed with super P with a mass ratio of 70:30. The mixture was further dispersed into NMP with PVDF binder (mixture: PVDF = 90:10, w/w) and cast with a doctor blade on Al foil. After drying in a vacuum oven at 40 °C for 1 day, the cathode was cut into Φ13 mm diameter round electrodes with a sulfur loading of around 1.0 mg/cm^2.

Electrochemical Characterization. The 2032-type coin cell was used to investigate the electrochemical performance of the modified separator. The cathode was the as-prepared sulfur electrode, and the anode was the lithium foil. 1 M LiTFSI in DME and DOL (1:1, v/v) with 0.4 M $LiNO_3$ additive was used as the electrolyte. The batteries were assembled in the Ar-filled glovebox in which the moisture and oxygen were controlled below 0.1 ppm. The cell performance tests were carried out using BT2043 Arbin Instruments, USA.

ASSOCIATED CONTENT

Supporting Information

TThe Supporting Information is available free of charge on the ACS Publications website at DOI: 10.1021/acsnano.7b08223.

Optical micrographs and related AFM images, effect of Hbim/toluene solution on thickness and size of the ZBCP sheets, STM images, XRF energy spectra, elemental analyses, SAED patterns, XRD profiles, N_2 and He adsorption-desorption isotherms and curves, AFM images, contact angle measurements, solubility tests, charge-discharge curves, cyclic voltammetry profiles, Nyquist analysis, cycling performance, SEM images, FTIR spectra, EDX element analysis, sulfur elemental mapping, polysulfide diffusion tests, photo of the setup used for the polysulfide permeation tests, and surface pressure-area isotherm (PDF)

AUTHOR INFORMATION

Corresponding Authors

*E-mail: jingkai.huang@kaust.edu.sa.
*E-mail: sean.li@unsw.edu.au.
*E-mail: lance.li@kaust.edu.sa.

ORCID

U-Ser Jeng: 0000-0002-2247-5061
Jun Ming: 0000-0001-9561-5718
Aram Amassian: 0000-0002-5734-1194
Zhiping Lai: 0000-0001-9555-6009
Yu Han: 0000-0003-1462-1118
Lain-Jong Li: 0000-0002-4059-7783

Author Contributions

○J.-K.H. and M.L. contributed equally to this work.

Notes

The authors declare no competing financial interest.

DOI: 10.1021/acsnano.7b08223
ACS Nano 2018, 12, 836−843

ACKNOWLEDGMENTS

L.-J.L. acknowledges support from the Competitive Research Grant (CRG; URF/1/2634-01) and Center Competitive Funding (CCF) from Solar Center, King Abdullah University of Science and Technology (Saudi Arabia). Z.L. and Y.H. acknowledge support from the Competitive Research Grant (CRG: URF/1/1723) and Competitive Research Grant (CRG; URF/1/2570-01-01), respectively, from King Abdullah University of Science and Technology (Saudi Arabia).

REFERENCES

(1) Liu, W.; Luo, X.; Bao, Y.; Liu, Y. P.; Ning, G.-H.; Abdelwahab, I.; Li, L.; Nai, C. T.; Hu, Z. G.; Zhao, D.; Liu, B.; Quek, S.; Loh, K. A Two-Dimensional Conjugated Aromatic Polymer *via* C−C Coupling Reaction. *Nat. Chem.* **2017**, *9*, 563−570.

(2) Vyas, V. S.; Haase, F.; Stegbauer, L.; Savasci, G.; Podjaski, F.; Ochsenfeld, C.; Lotsch, B. V. A Tunable Azine Covalent Organic Framework Platform for Visible Light-induced Hydrogen Generation. *Nat. Commun.* **2015**, *6*, 8508.

(3) Wu, Z.-S.; Zheng, Y.; Zheng, S.; Wang, S.; Sun, C.; Parvez, K.; Ikeda, T.; Bao, X.; Müllen, K.; Feng, X. Stacked-Layer Heterostructure Films of 2D Thiophene Nanosheets and Graphene for High-Rate All-Solid-State Pseudocapacitors with Enhanced Volumetric Capacitance. *Adv. Mater.* **2017**, *29*, 1602960.

(4) Zhao, S.; Wang, Y.; Dong, J.; He, C.-T.; Yin, H.; An, P.; Zhao, K.; Zhang, X.; Gao, C.; Zhang, L.; Lv, J.; Wang, J.; Zhang, J.; Khattak, A. M.; Khan, N. A.; Wei, Z.; Zhang, J.; Liu, S.; Zhao, H.; Tang, Z. Ultrathin Metal−Organic Framework Nanosheets for Electrocatalytic Oxygen Evolution. *Nat. Energy* **2016**, *1*, 16184.

(5) Peng, Y.; Li, Y. S.; Ban, Y. J.; Jin, H.; Jiao, W. M.; Liu, X. L.; Yang, W. S. Metal-organic Framework Nanosheets as Building Blocks for Molecular Sieving Membranes. *Science* **2014**, *346*, 1356−1359.

(6) Rodenas, T.; Luz, I.; Prieto, G.; Seoane, B.; Miro, H.; Corma, A.; Kapteijn, F.; Llabrés i Xamena, F. X.; Gascon, J. Metal−Organic Framework Nanosheets in Polymer Composite Materials for Gas Separation. *Nat. Mater.* **2015**, *14*, 48−55.

(7) Kanoo, P.; Ghosh, A. C.; Cyriac, S. T.; Maji, T. K. A Metal−Organic Framework with Highly Polar Pore Surfaces: Selective CO_2 Adsorption and Guest-Dependent On/Off Emission Properties. *Chem. - Eur. J.* **2012**, *18*, 237−244.

(8) Kim, J.; Kim, D. O.; Kim, D. W.; Sagong, K. Synthesis of MOF Having Hydroxyl Functional Side Groups and Optimization of Activation Process for the Maximization of Its BET Surface Area. *J. Solid State Chem.* **2013**, *197*, 261−265.

(9) Bunck, D. N.; Dichtel, W. R. Bulk Synthesis of Exfoliated Two-Dimensional Polymers Using Hydrazone-Linked Covalent Organic Frameworks. *J. Am. Chem. Soc.* **2013**, *135*, 14952−14955.

(10) Kissel, P.; Murray, D. J.; Wulftange, W. J.; Catalano, V. J.; King, B. T. A Nanoporous Two-Dimensional Polymer by Single-Crystal-to-Single-Crystal Photopolymerization. *Nat. Chem.* **2014**, *6*, 774−8.

(11) Falcaro, P.; Okada, K.; Hara, T.; Ikigaki, K.; Tokudome, Y.; Thornton, A. W.; Hill, A. J.; Williams, T.; Doonan, C.; Takahashi, M. Centimetre-Scale Micropore Alignment in Oriented Polycrystalline Metal-Organic Framework Films *via* Heteroepitaxial Growth. *Nat. Mater.* **2017**, *16*, 342−348.

(12) Makiura, R.; Motoyama, S.; Umemura, Y.; Yamanaka, H.; Sakata, O.; Kitagawa, H. Surface Nano-Architecture of a Metal−Organic Framework. *Nat. Mater.* **2010**, *9*, 565−571.

(13) Sahabudeen, H.; Qi, H.; Glatz, B. A.; Tranca, D.; Dong, R.; Hou, Y.; Zhang, T.; Kuttner, C.; Lehnert, T.; Seifert, G.; Kaiser, U.; Fery, A.; Zheng, Z.; Feng, X. Wafer-Sized Multifunctional Polyimine-Based Two-Dimensional Conjugated Polymers with High Mechanical Stiffness. *Nat. Commun.* **2016**, *7*, 13461.

(14) Sakamoto, R.; Hoshiko, K.; Liu, Q.; Yagi, T.; Nagayama, T.; Kusaka, S.; Tsuchiya, M.; Kitagawa, Y.; Wong, W. Y.; Nishihara, H. A Photofunctional Bottom-up Bis(dipyrrinato)zinc(II) Complex Nanosheet. *Nat. Commun.* **2015**, *6*, 6713.

(15) Xu, H.-J.; Liu, Y.-X.; Shen, Z.; Tian, Y.-Q.; You, X.-Z. $\{[Zn_2(Bim)_3(OH)(H_2O)]\cdot(DMF)(H_2O)_3\}_\infty$: A Two Dimensional Coordination Polymer with Layer Silicate-Like Structure. *Z. Anorg. Allg. Chem.* **2005**, *631*, 1349−1351.

(16) Deng, N.; Kang, W.; Liu, Y.; Ju, J.; Wu, D.; Li, L.; Hassan, B. S.; Cheng, B. A Review on Separators for Lithium Sulfur Battery: Progress and Prospects. *J. Power Sources* **2016**, *331*, 132−155.

(17) Zhou, G.; Pei, S.; Li, L.; Wang, D. W.; Wang, S.; Huang, K.; Yin, L. C.; Li, F.; Cheng, H. M. A Graphene−Pure-Sulfur Sandwich Structure for Ultrafast, Long-Life Lithium−Sulfur Batteries. *Adv. Mater.* **2014**, *26*, 625−631.

(18) Abbas, S. A.; Ibrahem, M. A.; Hu, L.-H.; Lin, C.-N.; Fang, J.; Boopathi, K. M.; Wang, P.-C.; Li, L.-J.; Chu, C.-W. Bifunctional Separator as a Polysulfide Mediator for Highly Stable Li−S Batteries. *J. Mater. Chem. A* **2016**, *4*, 9661−9669.

(19) Bai, S.; Liu, X.; Zhu, K.; Wu, S.; Zhou, H. Metal−Organic Framework-Based Separator for Lithium−Sulfur Batteries. *Nat. Energy* **2016**, *1*, 16094.

(20) Chung, S.-H.; Manthiram, A. High-Performance Li−S Batteries with an Ultra-Lightweight MWCNT-Coated Separator. *J. Phys. Chem. Lett.* **2014**, *5*, 1978−1983.

(21) Sun, J.; Sun, Y.; Pasta, M.; Zhou, G.; Li, Y.; Liu, W.; Xiong, F.; Cui, Y. Entrapment of Polysulfides by a Black-Phosphorus-Modified Separator for Lithium−Sulfur Batteries. *Adv. Mater.* **2016**, *28*, 9797−9803.

(22) Huang, J.-Q.; Zhang, Q.; Peng, H.-J.; Liu, X.-Y.; Qian, W.-Z.; Wei, F. Ionic Shield for Polysulfides Towards Highly-Stable Lithium−Sulfur Batteries. *Energy Environ. Sci.* **2014**, *7*, 347−353.

(23) Li, Z.; Jiang, Q.; Ma, Z.; Liu, Q.; Wu, Z.; Wang, S. Oxygen Plasma Modified Separator for Lithium Sulfur Battery. *RSC Adv.* **2015**, *5*, 79473−79478.

(24) Zhang, S. S.; Tran, D. T.; Zhang, Z. Poly (acrylic acid) Gel as a Polysulphide Blocking Layer for High-Performance Lithium/sulphur Battery. *J. Mater. Chem. A* **2014**, *2*, 18288−18292.

(25) Bruce, P. G.; Freunberger, S. A.; Hardwick, L. J.; Tarascon, J.-M. Li-O_2 and Li-S Batteries with High Energy Storage. *Nat. Mater.* **2012**, *11*, 19−29.

(26) He, M.; Yao, J.; Liu, Q.; Zhong, Z.; Wang, H. Toluene-Assisted Synthesis of RHO-Type Zeolitic Imidazolate Frameworks: Synthesis and Formation Mechanism of ZIF-11 and ZIF-12. *Dalton Trans.* **2013**, *42*, 16608−16613.

(27) Mohan, S.; Sundaraganesan, N.; Mink, J. FTIR and Raman Studies on Benzimidazole. Spectrochim. *Acta, Part A* **1991**, *47*, 1111−1115.

(28) Hu, Y.; Kazemian, H.; Rohani, S.; Huang, Y.; Song, Y. *In Situ* High Pressure Study of ZIF-8 by FTIR Spectroscopy. *Chem. Commun.* **2011**, *47*, 12694−12696.

(29) Kloprogge, J. T.; Hickey, L.; Frost, R. L. FT-Raman and FT-IR Spectroscopic Study of Synthetic Mg/Zn/Al-Hydrotalcites. *J. Raman Spectrosc.* **2004**, *35*, 967−974.

(30) Srivastava, O.; Secco, E. Studies on Metal Hydroxy Compounds. II. Infrared Spectra of Zinc Derivatives ϵ-$Zn(OH)_2$, β-ZnOHCl, ZnOHF, $Zn_5(OH)_8Cl_2$, and $Zn_5(OH)_8Cl_2\cdot H_2O$. *Can. J. Chem.* **1967**, *45*, 585−588.

(31) Sanchez, R. M. T.; Genet, M. J.; Gaigneaux, E. M.; Afonso, M. D.; Yunes, S. Benzimidazole Adsorption on the External and Interlayer Surfaces of Raw and Treated Montmorillonite. *Appl. Clay Sci.* **2011**, *53*, 366−373.

(32) Strohmeier, B.; Evans, W.; Schrall, D. Preparation and Surface Characterization of Zincated Aluminium Memory-Disc Substrates. *J. Mater. Sci.* **1993**, *28*, 1563−1572.

(33) Sun, R.-D.; Nakajima, A.; Fujishima, A.; Watanabe, T.; Hashimoto, K. Photoinduced Surface Wettability Conversion of ZnO and TiO_2 Thin Films. *J. Phys. Chem. B* **2001**, *105*, 1984−1990.

(34) Degen, A.; Kosec, M. Effect of PH and Impurities on the Surface Charge of Zinc Oxide in Aqueous Solution. *J. Eur. Ceram. Soc.* **2000**, *20*, 667−673.

DOI: 10.1021/acsnano.7b08223
ACS Nano 2018, 12, 836−843

(35) Sundberg, R. J.; Martin, R. B. Interactions of Histidine and Other Imidazole Derivatives with Transition Metal Ions in Chemical and Biological Systems. *Chem. Rev.* **1974**, *74*, 471−517.
(36) Hunter, R. J. *Zeta Potential in Colloid Science*; Academic Press: New York, 1981; Vol. 2.
(37) De Oliveira, E.; Hase, Y. Infrared Study and Isotopic Effect of Magnesium Hydroxide. *Vib. Spectrosc.* **2001**, *25*, 53−56.
(38) Dhaouadi, H.; Chaabane, H.; Touati, F. $Mg(OH)_2$ Nanorods Synthesized by a Facile Hydrothermal Method in the Presence of CTAB. *Nano-Micro Lett.* **2011**, *3*, 153−159.
(39) Li, M.; Wahyudi, W.; Kumar, P.; Wu, F.; Yang, X.; Li, H.; Li, L.-J.; Ming, J. Scalable Approach To Construct Free-Standing and Flexible Carbon Networks for Lithium−Sulfur Battery. *ACS Appl. Mater. Interfaces* **2017**, *9*, 8047−8054.
(40) Mikhaylik, Y. V.; Akridge, J. R. Polysulfide Shuttle Study in the Li/S Battery System. *J. Electrochem. Soc.* **2004**, *151*, A1969−A1976.
(41) Zhang, S. S. Liquid Electrolyte Lithium/sulfur Battery: Fundamental Chemistry, Problems, and Solutions. *J. Power Sources* **2013**, *231*, 153−162.
(42) Domańska, U.; Pobudkowska, A.; Rogalski, M. Solubility of Imidazoles, Benzimidazoles, and Phenylimidazoles in Dichloromethane, 1-chlorobutane, Toluene, and 2-nitrotoluene. *J. Chem. Eng. Data* **2004**, *49*, 1082−1090.

DOI: 10.1021/acsnano.7b08223
ACS Nano 2018, 12, 836−843